Coastal Engineering 94 (2014) 47–62

Contents lists available at ScienceDirect

Coastal Engineering

journal homepage: www.elsevier.com/locate/coastaleng

Wave attenuation in mangroves: A quantitative approach to field observations

E.M. Horstman [a,b,*,1], C.M. Dohmen-Janssen [a,1], P.M.F. Narra [c,2], N.J.F. van den Berg [b,d,3,4], M. Siemerink [b,d,5,6], S.J.M.H. Hulscher [a,1]

[a] Water Engineering and Management, University of Twente, P.O. Box 217, 7500 AE Enschede, The Netherlands
[b] Singapore-Delft Water Alliance, National University of Singapore, Engineering Drive 2, 117576 , Singapore
[c] Departamento de Engenharia Civil, Universidade de Aveiro, Campus Universitário de Santiago, 3810-193 Aveiro, Portugal
[d] Water Engineering and Management, University of Twente, The Netherlands

ARTICLE INFO

Article history:
Received 21 January 2014
Received in revised form 6 August 2014
Accepted 8 August 2014
Available online 19 September 2014

Keywords:
Mangroves
Vegetation density
Wave attenuation
Sediment deposition

ABSTRACT

Coastal mangroves, dwelling at the interface between land and sea, provide an important contribution to reducing risk from coastal hazards by attenuating incident waves and by trapping and stabilizing sediments. This paper focusses on relations between vegetation densities, wave attenuation rates, sediment characteristics and sedimentation rates in mangroves. These processes were studied along two cross-shore transects through mangroves fringing estuaries in the southern Andaman region of Thailand. Volumetric vegetation densities in these mangroves were ranging up to 32‰, depending on the water depth. Generalized total wave attenuation rates increased from 0.002 m^{-1} in the sparsely vegetated forest fringes with *Avicennia* and *Sonneratia* species, up to 0.012 m^{-1} in the dense *Rhizophora* vegetation in the back of the forests. The total wave attenuation rates integrate effects of shoaling and energy losses due to various bio-physical interactions within the mangrove ecosystem. Wave attenuation in the mangroves is presumably dominated by energy losses due to vegetation drag, since wave attenuation due to bottom friction and viscous dissipation on the bare mudflats is significantly lower than those inside the mangrove vegetation.

Additionally, wave attenuation in the mangroves was found to facilitate enhanced net sediment deposition and a gradual fining of the bed material. These findings corroborate the coastal defence function of mangroves by quantifying their contribution to wave attenuation and sediment trapping. The explicit linking of these properties to vegetation composition and structure facilitates modelling studies investigating the mechanisms determining the coastal defence capacities of mangroves.

1. Introduction

Mangroves are a key-ecosystem dwelling in the intertidal area of tropical and sub-tropical coastlines. Mangrove vegetation, consisting of trees and shrubs, copes with the harsh conditions in the intertidal: salinity, tidal flooding and exposure to waves. Forming an evident buffer between land and sea, often in areas lacking robust sea defences, mangroves contribute to wave attenuation (Quartel et al., 2007; Vo-Luong and Massel, 2006) and to coastal stabilization (Alongi, 2008; Anthony, 2004; Augustinus, 1995; Van Santen et al., 2007). Mangroves are even said to have saved lives and properties during the Indian Ocean tsunami in 2004 (Danielsen et al., 2005; Kathiresan and Rajendran, 2005), though the exact contribution of mangrove vegetation is disputed (Kerr et al., 2006). Despite these invaluable regulating services, mangroves are in rapid decline (FAO, 2007; Spalding et al., 2010). Hence, there is an urgent need to unravel the physical contribution of mangroves to reducing risk from coastal hazards in order to increase awareness of the need for mangrove preservation.

Unravelling the dissipation of wave energy in coastal mangroves by field and laboratory studies has only gained attention since the late nineties (Alongi, 2009). Due to the inaccessibility of (natural) mangrove forests, a limited number of field studies has been executed in mangroves in Vietnam, Australia and Japan (Table 1). These studies emphasize in unison the positive contribution of mangroves to the dissipation of

* Corresponding author at: Water Engineering and Management, University of Twente, P.O. Box 217, 7500 AE Enschede, The Netherlands. Tel.: +31 53 489 3546.
E-mail addresses: E.M.Horstman@utwente.nl (E.M. Horstman), C.M.Dohmen-Janssen@utwente.nl (C.M. Dohmen-Janssen), PedroNarra@ua.pt (P.M.F. Narra), Niels-Jasper.van.den.Berg@rhdhv.com (N.J.F. van den Berg), Martijn.Siemerink@nelen-schuurmans.nl (M. Siemerink), S.J.M.H.Hulscher@utwente.nl (S.J.M.H. Hulscher).
[1] Tel.: +31 53 489 3546.
[2] Tel.: +351 234 370 098.
[3] Tel.: +31 10 443 3666.
[4] Currently at Royal HaskoningDHV, P.O. Box 8520, 3009 AM Rotterdam, The Netherlands.
[5] Tel.: +31 30 233 0200.
[6] Currently at Nelen & Schuurmans, P.O. Box 1219, 3500 BE Utrecht, The Netherlands.

http://dx.doi.org/10.1016/j.coastaleng.2014.08.005
0378-3839/

wind and swell waves of limited height and period. Nevertheless, observed wave reduction rates show significant variation with water depth and vegetation characteristics (Table 1).

Wave attenuation by mangroves observed in the field has previously been parameterized by calculating bulk roughness parameters, either a wave attenuation rate (Table 1) or a bulk drag coefficient, comprising both vegetation induced drag forces and bottom friction (Mazda et al., 1997a; Quartel et al., 2007). Both Mazda et al. (1997a) and Quartel et al. (2007) obtained exponentially increasing bulk drag coefficients for increasing water depths within the mangroves due to limited height of the dwarfed trees in their field sites. Conversely, Brinkman et al. (1997) obtained increasing transmission factors, hence decreasing wave attenuation, for increasing water depths at two sites with taller mangrove vegetation (Table 1).

Enhancing understanding of the contributing processes determining wave attenuation in mangroves requires mechanistic studies of the propagation of waves through vegetation. Recent advances in numerical modelling explicitly resolve vegetation induced drag forces by integrating friction forces over a composition of one or several layers of rigid vertical cylinders (Suzuki et al., 2012; Vo-Luong and Massel, 2008). For a reliable representation of the vegetation, this approach compels detailed, site specific information on vegetation characteristics such as stem and root diameters, vertical vegetation distribution, vegetation densities and (bulk) drag coefficients. However, due to poor vegetation data the abovementioned models were calibrated in the vegetation parameters (Suzuki et al., 2012; Vo-Luong and Massel, 2008), raising questions regarding their general validity.

Field data comprising accurate measurements of both hydrodynamics (wave heights, water depths and, if possible, flow velocities) and vegetation parameters is indispensable for further development of the abovementioned numerical models (McIvor et al., 2012; Möller, 2012). Both hydrodynamics and vegetation parameters are changing from site to site, depending on local geography, wave climate and vegetation composition. Although wave attenuation studies accurately quantified hydrodynamic conditions, usually only a very limited range of conditions is covered as data collection often spans a few tides only (Brinkman, 2006; Mazda et al., 1997a). Vegetation characteristics were poorly represented in previous studies, by either qualitative descriptions of local vegetation patterns or fairly rough quantifications of the vegetation cover (Brinkman, 2006; Quartel et al., 2007; Vo-Luong and Massel, 2006). Mazda et al. (1997b) made an exceptional effort by identifying detailed vegetation parameters and quantifying the volume of submerged mangrove biomass. This concept will be deployed in the present paper.

This paper addresses the explicit correlations between vegetation densities, wave attenuation, sediment characteristics and sedimentation rates in mangroves. We aim to correlate the total wave attenuation through a mangrove system with the volume-percentage of submerged mangrove biomass for variable vegetation compositions and densities, pursuing an explicit relation between the mangrove density and the wave attenuation capacity of mangroves. Along with these bio-physical interactions, we aim to link the attenuated hydrodynamic conditions to sediment properties and deposition rates within mangroves. These correlations will be based on the results of a comprehensive field campaign along two cross-shore transects through mangrove fringes, combining measurements of the hydrodynamics and sediment dynamics at multiple positions along these transects with the collection of detailed topographic and vegetation data.

2. Study sites

The study sites are located in the fringing mangroves at the west coast of southern Thailand, in Trang Province (Fig. 1A,B). This area is part of the convoluted Thai Andaman coast, comprising numerous

Table 1
Overview of previous studies into wave attenuation in mangroves. Wave attenuation is quantified by the ratio of the wave height reduction (ΔH) and the incident wave height (ΔH) per distance (Δx): $r = \Delta H / (H \cdot \Delta x)$.

Location – Mangrove setting	Vegetation	Incident wave height H & period T	Wave attenuation
Tong King Delta, Vietnam – Fringing mangroves (Mazda et al., 1997a)	Sparse *Kandelia candel* seedlings (1/2 year-old), planted	H = – T = 5–8 s	r = 0.01–0.10 per 100 m
	Dense 2–3 year-old *Kandelia candel*, up to 0.5 m high, planted	H = – T = 5–8 s	r = 0.08–0.15 per 100 m
	Dense 5–6 year-old *Kandelia candel*, up to 1 m high, planted	H = – T = 5–8 s	r = 0.15–0.22 per 100 m
Vinh Quang, Vietnam – Fringing mangroves (Mazda et al., 2006)	*Sonneratia* sp., 20 cm high pneumatophores, canopy starts 60 cm above bed, planted	H = 0.11–0.16 m T = 8–10 s	r = 0.002–0.006 m^{-1}
	No vegetation	H = 0.11–0.16 m T = 8–10 s	r = 0.001–0.002 m^{-1}
Can Gio, Vietnam – Riverine mangroves (Vo-Luong and Massel, 2006)	Mixed *Avicennia* sp. and *Rhizophora* sp.	H = 0.35–0.4 m T = – s	Energy reduction factor = 0.50–0.70 over 20 m (including a cliff)
Do Son, Vietnam – Fringing mangroves (Quartel et al., 2007)	Mainly *Kandelia candel* bushes and small trees	H = 0.15–0.25 m T = 4–6 s	r = 0.004–0.012 m^{-1}
	Non-vegetated beach plain	H = 0.15–0.25 m T = 4–6 s	r = 0.0005–0.002 m^{-1}
Red River Delta, Vietnam – Fringing (?) mangroves (Bao, 2011)	Mixed vegetation	H = 0.15–0.27 m T = – s	r = 0.0055–0.01 m^{-1}
Can Gio, Vietnam – Fringing (?) mangroves (Bao, 2011)	Mixed vegetation	H ~ 0.55 m T = – s	r = 0.017 m^{-1}
Cocoa Creek, Australia – Fringing mangroves (Brinkman, 2006; Brinkman et al., 1997)	Zonation: *Rhizophora* sp. (front), *Aegiceras* sp., *Ceriops* sp. (back)	H = 0.01–0.07 m T ~ 2 s	Energy transmission factor =0.45–0.80 over 160 m
Iriomote, Japan – Riverine mangroves (Brinkman, 2006; Brinkman et al., 1997)	*Bruguiera* sp., 20–30 cm high knee roots	H = 0.08–0.15 m T ~ 2 s	Energy transmission factor =0.15–0.75 over 40 m
Oonoonba, Australia – Fringing mangroves (Brinkman, 2006)	Zonation: *Sonneratia* sp. (front) and *Rhizophora* sp. (back)	H = 0.04–0.25 m T ~ 6 s	Energy reduction factor =0.9–1.0 over 40 m

embayments, islands and islets offering a perfect habitat to mangroves. The Andaman coast hosts about 80% of the 244,000 ha of Thai mangroves (FAO, 2007). Although the Thai Andaman coast was severely struck by the 2004 Indian Ocean tsunami, the study sites remained unaffected. The tip of Sumatra (Banda Aceh) and the many islets shelter the southern part of the Andaman Sea and the study sites, respectively, from incoming waves from the Indian Ocean.

Two cross-shore transects were defined for this study. One transect was located in the district of Kantang, within the estuary of the rivers Mae Nam Trang and Khlong Palian, herein referred to as the Kantang estuary (Fig. 1C). The other transect was situated in the district of Palian, within the estuary with the Khlong Lak Khan and Khlong Rae as its tributaries, herein referred to as the Palian estuary (Fig. 1D). The Kantang transect was directed southwest towards the Andaman Sea (Fig. 1C) while the Palian transect was directed towards the southeast across the Palian River estuary (Fig. 1D). These cross-shore transects were aligned with the prevailing direction of wave propagation in the shallow coastal waters. We focussed on the front few 100's of metres, of the rather extensive mangrove forests in both estuaries as attenuation of hydrodynamic energy largely occurs in the mangrove fringes.

Both transects featured a gradually sloping forest floor with average slopes of 3.3(±2.6):1000 and 6.0(±7.6):1000 (±standard deviations) for the Kantang and Palian transect, respectively (Fig. 2). The sparsely vegetated forest front at both transects was dominated by trees of *Avicennia* sp. and *Sonneratia* sp. (Fig. 2) and the forest floor was covered in a dense layer of pneumatophores (pencil roots) of these trees. The densely vegetated back forest at both transects was dominated by *Rhizophora* sp. instead, with dense networks of stilt roots. Due to the difference in bed slopes and the inundation induced zonation of mangrove vegetation (Van Loon et al., 2007; Watson, 1928), the vegetation zones were narrower along the Palian transect than along the Kantang transect. Additionally, greater vegetation densities were observed in the Palian back forest.

The study sites were tide dominated (Woodroffe, 1992), both exposed to a similar mixed semi-diurnal tide with a mean tidal range of 2.0 m and a maximum range of 3.6 m (Horstman et al., 2013). The wind wave climate in this region is largely imposed by the monsoons. Southwest monsoons generate the highest waves at the Andaman coast and prevail from May to October. Northeast monsoons prevail from October to February. The present data were collected from December 2010 to May 2011 and hence mainly cover the relatively quiescent conditions of the northeast monsoon. However, during the last week of March 2011, the Andaman coast was struck by severe storms giving rise to increased wave heights at the coasts and causing severe inland floods. Additionally, wave exposure of the two transects varied due to the different orientations with respect to the Andaman Sea (Fig. 1C,D).

3. Data collection and processing

3.1. Elevation survey

We mapped the topography of the study sites thoroughly with Trimble survey equipment (SPS 700-S6 Total Station and R-6 Real Time Kinematic GPS). At each transect about 100 survey points were collected with respect to local benchmarks. Survey point densities were increased in steeper sloping (vegetated) parts of the transects. The local benchmark at each transect was georeferenced with an RTK-GPS. The elevation of the transects with respect to mean sea level was obtained from an analysis of locally obtained tidal water level data (Section 3.3). These elevation data were processed to cross-shore profiles of the transects (Horstman et al., 2013).

3.2. Vegetation survey

Vegetation cover at the wave transects was mapped by quantifying all vegetation elements within a total of six vegetation plots of 20×20 m^2 along both transects. These plots were distributed over the vegetation zones along both transects and according to the spacing and vegetation variability, one or two plots were assigned per zone (Fig. 1C,D). The vegetation survey method slightly differed for the plots within the sparsely vegetated front forest and the plots within the densely vegetated back forest.

In the forest fringe (plots TKI^{a,b} and TPI in Fig. 2), where *Avicennia* and *Sonneratia* species were predominant (Fig. 4B), trees were classified according to their stem diameter. The stem diameter was measured at breast height (i.e. 1.50 m) or, when the tree was too small, at one third of the height of the sapling. These stem diameters were categorized in five groups: 0–10 mm, 10–25 mm, 25–100 mm, 100–200 mm and >200 mm. Per category, one representative tree was then selected of which the stem diameter was measured at 0.1 m, 0.5 m, 1.0 m, 1.5 m and 2.0 m above the bed. Diameters of branches at these elevations, if any, were included as well. *Rhizophora* vegetation in the forest fringe was rather sparse and those trees present were quite similar and small. All *Rhizophora* trees in the plots were counted and diameters of all roots, stems and branches of one representative tree were measured at the same elevations above the bed.

In the densely vegetated back forest (plots TKII^{a,b} and TPII in Fig. 2), *Rhizophora* sp. was predominant (Fig. 4C). In these plots, all trees were counted and root characteristics were measured for a small, an average and a large tree (*Rhizophora* tree sizes were much more variable than in the forest fringe). Detailed characterization of these trees was performed similar to the method for the forest fringe: diameters of all roots, stems and branches of the representative trees were measured

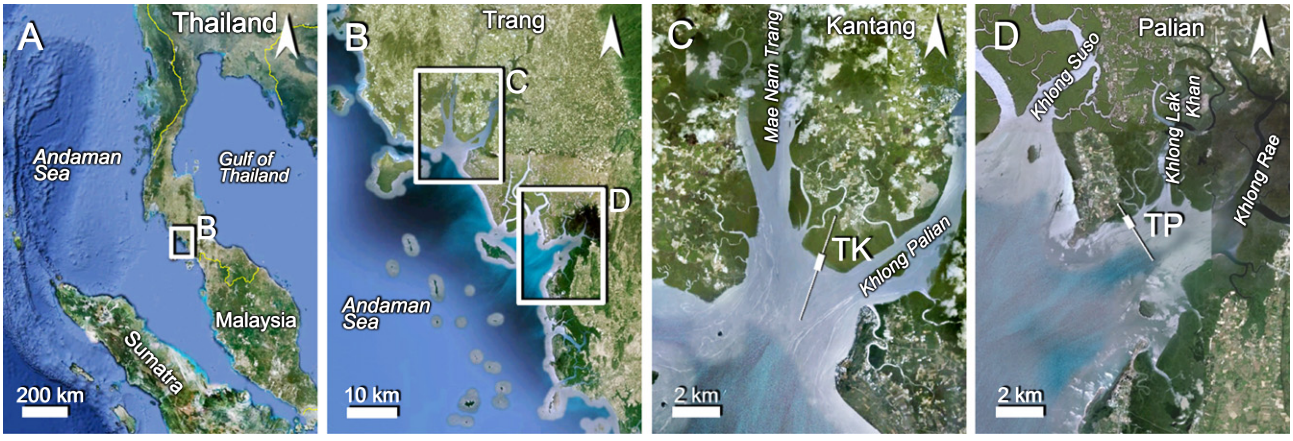

Fig. 1. Topography of the study sites. (A) The west coast of southern Thailand facing the Andaman Sea. (B) The coastal areas of Trang province. (C) The Kantang estuary with the position and orientation of the Kantang transect (TK) indicated by a box and a line, respectively. (D) The Palian estuary with the Palian transect (TP) indicated similarly. (imagery: Google Earth).

at 0.1 m, 0.5 m, 1.0 m and 2.0 m above the bed. *Avicennia* and *Sonneratia* trees in the back forest were treated similar to the *Rhizophora* trees: their total number was counted and the same data were collected for representative samples.

Seedlings (i.e. single stemmed tree saplings) were only encountered in plot TPII and these were counted separately, along with the diameter of one average seedling sample. For remaining stems of dead trees, the average height and diameter were included in the vegetation data as well. Additionally, three subplots of 0.5×0.5 m^2 (or 1×1 m^2, depending on pneumatophore densities) were allocated within each vegetation plot, representing a sparse, average and dense pneumatophore cover. In each subplot, the total number of pneumatophores was counted. Height and diameter of the pneumatophores were measured for 20 randomly chosen pneumatophores per subplot.

These detailed vegetation data were transformed into spatially explicit vegetation densities. Vegetation data was first transformed into the total horizontal coverage of vegetation elements within each of the vegetation plots at different levels above the bed. Subsequently, the volume of vegetation within a water column of arbitrary depth was calculated by integrating the (depth-dependent) horizontal vegetation coverage over this depth. The vegetation density was then expressed as the relative vegetation volumes (volume-‰) compared to the total submerged volume, similar to the volumetric vegetation parameter deployed by Mazda et al. (1997b).

3.3. Hydrodynamic data collection

Six high-frequency pressure sensors (MacroWave, Coastal Leasing Inc.) were deployed for collecting wave data along the transects. These sensors are robust and the internal memory and battery housing facilitates autonomous data collection for periods of up to several weeks, depending on sampling frequency and battery quality. Sampling rates of the pressure sensors were set to 10 Hz, with burst lengths of 2^{12} samples (~7 min) at intervals of 20 min. Data collection by all sensors started simultaneously for every deployment. To start data collection at shallow water depths, the instruments were buried with the sensors levelled at 5–7 cm above the bed (Fig. 3).

The wave sensors were deployed at six positions along each of the wave transects (Fig. 2). Two sensors were located at the consecutive interfaces between the mudflat, the sparsely vegetated forest fringe and the densely vegetated back forest (Fig. 3). The four remaining sensors were located within these zones: one on the mudflat in front of the forest, one in the sparsely vegetated forest fringe and two within the densely vegetated back forest (Fig. 2). Following the different topography of the sites, distances between the instrument locations were about 50 m along the Kantang transect (Fig. 2A) and about 20 m at the Palian transect (Fig. 2B).

Wave sensors were deployed three times along each transect and single deployments lasted for periods of 2 to 6 weeks. Deployments at the Kantang transect spanned: 26 January to 5 March, 7 March to 20 March and 24 March to 14 April 2011. At the Palian transect, instrument deployments covered: 25 November to 5 December 2010, 8 December 2010 to 19 January 2011 and 17 April to 2 May 2011. Due to poor battery performance and technical issues, some sensors stopped data collection prior to the planned end date. Hence, collected data is gapped in time and space.

Next to these high-frequency wave sensors, low-frequency pressure (and temperature) loggers (Sensus Ultra, ReefNet Inc.) were deployed continuously during the field campaign. These sensors collected pressure data with a sampling interval of 5 min, monitoring tidal water levels. These loggers were positioned at K2 along the Kantang transect and between P2 and P3 at the Palian transect (Fig. 2).

3.4. Sediment data collection

Sediment deposition was monitored with sediment traps. The traps were made of 0.20×0.25 m^2 ceramic tiles, covered in a smooth layer of mortar to mimic the forest floor. These tiles were carefully levelled with the forest floor (Fig. 3). This design allowed for both sediment deposition and entrainment, providing net sediment deposition rates. Sediment traps were deployed during one single deployment at each transect. Two traps were deployed at each monitoring position along the transects during spring low tide (7 March at Kantang, 19 April at Palian). One trap of each pair was collected after a period of one or two tides (~12/24 h), the other trap was collected after a full spring–neap tidal cycle (20 March at Kantang, 2 May at Palian). Single-day sediment trapping during neap tidal conditions rendered inaccurate results as parts of the transects remained submerged at neap low tide.

Deposited sediments were rinsed, filtered (0.7 μm Whatman GF/F filters) and dried for 24 h at 105° before weighing (Horstman et al., 2011). Additionally, a sediment sample (20–30 cm^3) of the (undisturbed) top layer of the bed (3–4 cm) was collected at every monitoring position. These samples were analysed for grain size distributions (Malvern) and organic matter content (ashing).

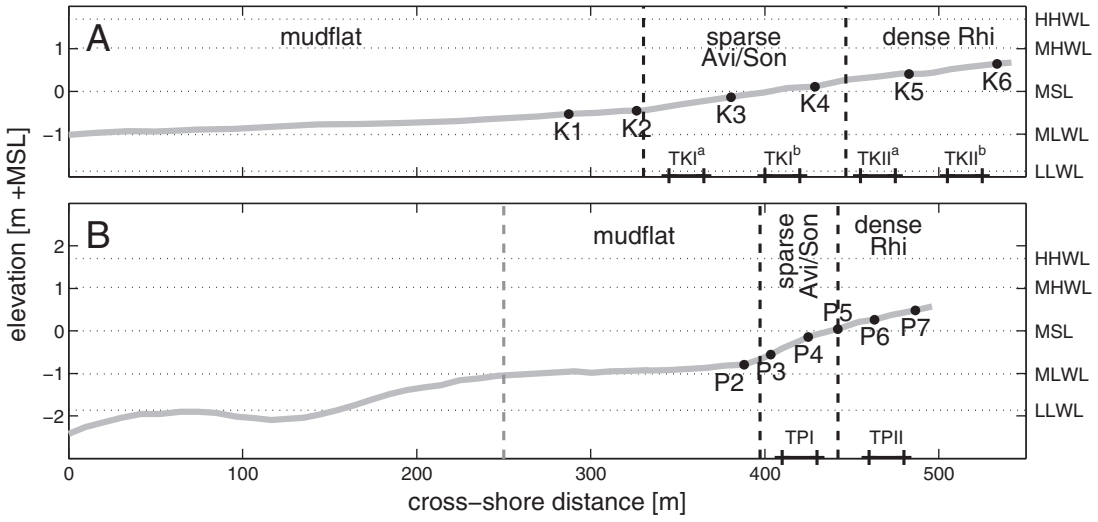

Fig. 2. Elevation with respect to mean sea level (MSL) of the cross-shore transects including instrument positions at (A) the Kantang transect and (B) the Palian transect. Distinct vegetation zones along the transects are demarcated by dashed lines (Avi/Son = *Avicennia/Sonneratia*; Rhi = *Rhizophora*). Plot positions of the vegetation survey are indicated at the bottom of each graph. Characteristic tidal water levels are indicated at the right axis (HHWL = highest high water level; MHWL = mean high water level; MLWL = mean low water level; LLWL = lowest low water level).

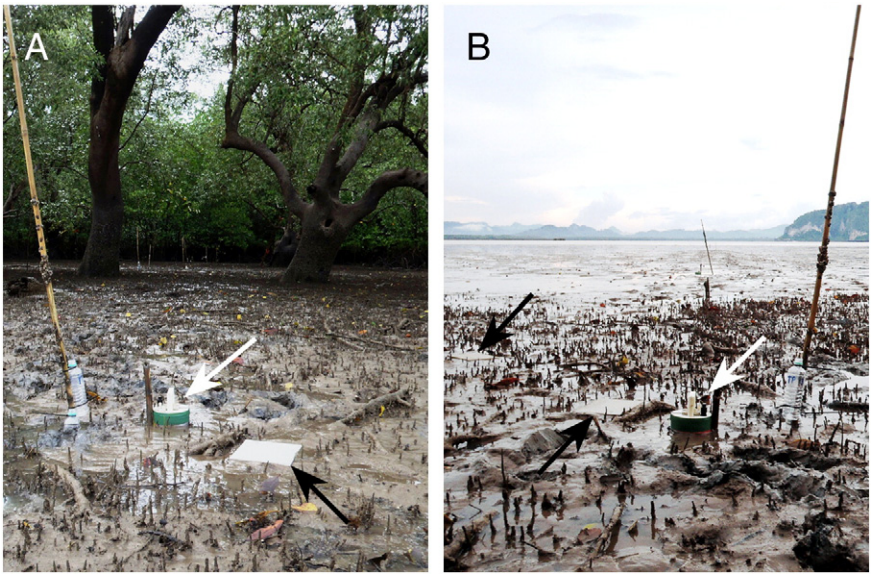

Fig. 3. Simultaneous deployment of wave sensors (white arrows) and sediment traps (black arrows) at the Palian transect, position P3. (A) A view towards the forest: the sparse *Avicennia* and *Sonneratia* vegetation landward of P3, and the dense *Rhizophora* forest in the back. (B) A view towards the estuary: P3 was located at the edge of the mangrove vegetation, with a mudflat in front of it.

3.5. Processing hydrodynamic data

Obtained pressure data from the wave sensors were corrected for the atmospheric pressure, preliminary to the conversion into water depths. Meteorological data for the period of the field campaign showed that the average atmospheric pressure was 1008 hPa. Diurnal fluctuations of the atmospheric pressure (±5 hPa) were irrelevant on the short time scale of waves. For the conversion of the corrected pressure data to water depths, the specific gravity of the water was calculated from the site specific gravitational acceleration and water density: 9.78 m/s^2 and 1004 kg/m^3 respectively. This density was computed for a water temperature varying between 26 and 33 °C (observed by the Sensus Ultra loggers) and a salinity of 9–13 PPT (obtained from water samples).

Spectral analysis of the obtained wave signal was executed according to Hegge and Masselink's (1996) Fourier analysis scheme, resulting in wave energy density spectra for each data burst (see Appendix A). From these energy density spectra, we derived the significant wave height H_s [m], root-mean-square wave height H_{rms} [m], mean wave period T_m [s] and total wave energy E_{tot} [J/m^2] for every burst of wave data. Subsequently, data bursts were selected for time spans during which the entire transect was flooded. This selection was due to assimilate coherent datasets of the wave characteristics at the consecutive monitoring positions along each transect, obtained simultaneously and for similar conditions (e.g. incoming wave height).

4. Results

4.1. Vegetation density

High-resolution vegetation data (see Appendix B) were transformed into vegetation cover rates, expressing the relative vegetation coverage of the horizontal surface at certain elevations (in per milles (‰), see Fig. 4A). At 5 cm above the bed (i.e. the mean height of the pneumatophores), vegetation coverage in the *Avicennia*/*Sonneratia* plots was quite high (17–23‰, Fig. 4A) due to the dense cover of pneumatophores varying from 300 up to 2200 pneumatophores/m^2 (Appendix B). Above this dense layer of pneumatophores, vegetation coverage suddenly decreased to less than 5‰, since at these levels vegetation mainly consisted of a few tree stems (Fig. 4B). For the *Rhizophora* plots, the near bed vegetation density was of the same order, although the coverage showed greater variability (15–41‰). The decrease of vegetation coverage with increasing elevation was much more gradual in this zone than in the forest fringe due to the characteristic architecture of these trees. The stilt roots of the *Rhizophora* trees branch off into a dense network of roots (up to 460 roots for a single large tree were counted) with a typical diameter of only a few centimetres close to the bed (Fig. 4C, Appendix B).

The horizontal vegetation coverage was integrated over the water depth to obtain the volumetric vegetation density (expressed as volume-‰). For the Palian transect, vegetation densities in the forest fringe were significantly smaller than in the back of the forest with volumetric densities of 4.3‰ and 20‰, respectively, for a water depth of 1 m. For the Kantang transect, for a water depth of 1 m, volumetric vegetation densities within both plots in the *Avicennia*/*Sonneratia* zone (hereafter indicated as the *Avicennia* zone) were 4.5‰, while the density was 5.8‰ and 9.3‰ for the front and back plots within the *Rhizophora* zone, respectively. The increase in vegetation density along the Kantang transect was much less pronounced and did not correlate as much to the predominant vegetation type as along the Palian transect, due to the sparser *Rhizophora* cover at the Kantang transect.

4.2. Wave climate

Time-averaged wave energy density spectra at all cross-shore monitoring positions are plotted in Fig. 5 for each deployment (periods with spectra for less than six positions are due to malfunctioning sensors). Obtained wave data cover a wide range of tidal conditions (Fig. 5I), although neap tides are poorly represented in the data as water levels remained too low to flood the entire transects. Data of the last deployment at Kantang and the middle deployment at Palian are separated in a high-energy period (Fig. 5D and F, respectively) and a period with moderate wave conditions (Fig. 5C and G, respectively). The wave energy density spectra at the front most monitoring positions at both transects were found to be independent of the local water depth.

In general, the observed wave energy was low during the first three periods of data collection (Fig. 5A,E,G), except for a few days early December (Fig. 5F) when wind directions turned onshore (southwest) instead of the usual offshore (northeast) wind direction for this time of the year (Thai Meteorological Department, 2012). These periods coincided

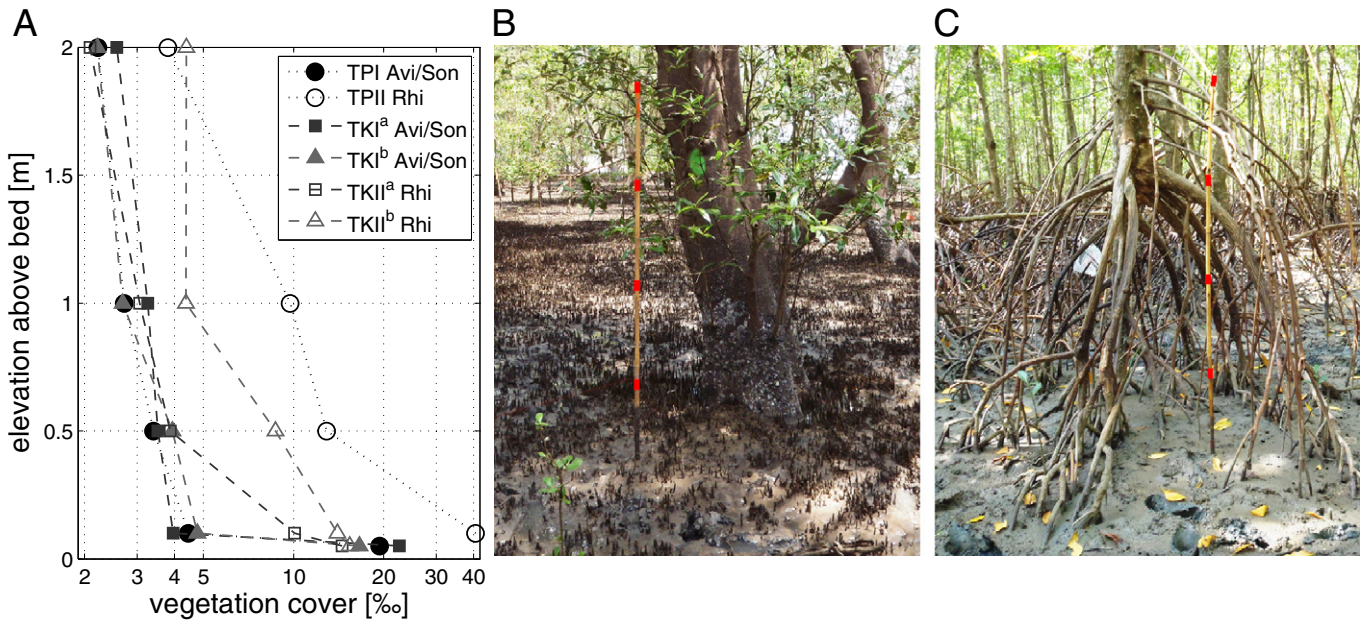

Fig. 4. Variation of the vegetation cover with elevation above the forest floor. (A) Horizontal vegetation coverage [‰] significantly reduces with increasing elevation above the forest floor. (B) Characteristic vegetation in the *Avicennia/Sonneratia* zone (TKI[b]). (C) Characteristic vegetation in the *Rhizophora* zone (TKII[b]). The marks on the bamboo in (B) and (C) are 0.50 m apart and start at 0.50 m above the bed.

with the northeast monsoon period, lasting until February. Wave energy increased during the subsequent deployments (Fig. 5B, C,D,H), upon the arrival of the southwest monsoon, starting in May. The most energetic conditions were observed in the March/April deployment at the Kantang transect (Fig. 5D), when the area was hit by severe storms.

The wave spectra for the Kantang transect were mostly uni-modal with wave periods mainly varying between either 6–11 s for the January/February deployment (Fig. 5A) and 11–19 s for the data collected in March and April (Fig. 5B–D). The wave spectra for the Palian transect, on the other hand, were less consistent. The spectra for the December and April/May measurements along this transect were bi-modal, with peaks at periods between 3–5 s and 6–11 s for the former period (Fig. 5F) and at periods between 6–10 s and 11–19 s for the latter period (Fig. 5H). The Kantang transect was typically exposed to swell waves (10–20 s) during the deployments in March and April, while the wave climate at the Palian transect was mostly dominated by shorter sea waves (<10 s). Although, at Palian the contribution of swell waves increased as well at the onset of the southwest monsoon.

Maximum energy densities along the Kantang transect were up to twice as high as the maxima along the Palian transect, indicating that the Kantang transect was exposed to higher waves. Together with the different modalities of the spectra, these characteristics were induced by the orientation of the transects. The Kantang transect was directly exposed to swell waves from the Andaman Sea and hence incident waves were at the lower end of the frequency spectrum for wind waves. The Palian transect, on the other hand, was oriented towards an estuary with a short fetch, limiting the period and height of the incident waves.

Energy density levels generally decreased at the consecutive sensors along the transects. Nevertheless, a local increase of the wave energy density in the swell wave regime is observed between the consecutive sensors during the March measurements at the Kantang transect (Fig. 5B) and during the December/January and April/May measurements at the Palian transect (Fig. 5G,H). Such an increase of the energy density of the low-frequency component of the energy density spectra can be induced by (i) enhanced shoaling of shorter waves and (ii) energy transfer to lower frequencies by nonlinear wave–wave interactions (Elgar and Raubenheimer, 2008).

4.3. Cross-shore changes in wave properties

Changes of the wave characteristics along the transects were obtained from the wave energy density spectra for each data collection period (Fig. 6). Typical incident waves at both transects (at K1 and P2) did not exceed 15 cm in height. No significant correlation was obtained between the water depths and the wave heights at K1 and P2 (Pearson's $R = 0.05$ ($p = 0.36$) and $R = 0.01$ ($p = 0.77$), respectively), hence depth-limitations were insignificant to the incident shallow waves.

Between the first and last sensors at the Kantang transect (K1–K6), mean significant wave heights gradually decreased from 5.5–10.6 cm to 2.9–5.8 cm (−42 to −47%; Fig. 6A). During the March deployment, wave height decreased from 6.7 to 4.6 cm (−31%) between K1 and K5 only. The increasing wave heights in the subsequent deployments coincide with the increase of the wave energy density spectra for the respective data series (Fig. 5A,B,C,D). Mean significant wave heights along the Palian transect decreased from 4.4–11.3 cm to 3.0–6.5 cm between the first and last sensors (−30 to −43%; Fig. 6I). A lower reduction, from 8.4 to 6.6 cm (−22%), was obtained between P2 and P6 during the last data series.

While the significant wave heights decreased along both transects, mean wave periods were slightly increasing towards the back of the forest. Mean wave periods changed from 2.9–6.4 s to 4.1–5.7 s and from 2.8–4.1 s to 4.8–5.0 s along the Kantang and Palian transects, respectively (Fig. 6B,J). This is corroborated by the wave energy density spectra presented in Fig. 5, showing that the shorter sea waves (i.e. frequencies >0.1 Hz) lost more energy when propagating into the forest than the longer swell waves (<0.1 Hz). Hence, shorter waves got attenuated more effectively when propagating into the forest, as opposed to the longer-period swell waves that hardly got attenuated, giving rise to an increase of the mean wave periods.

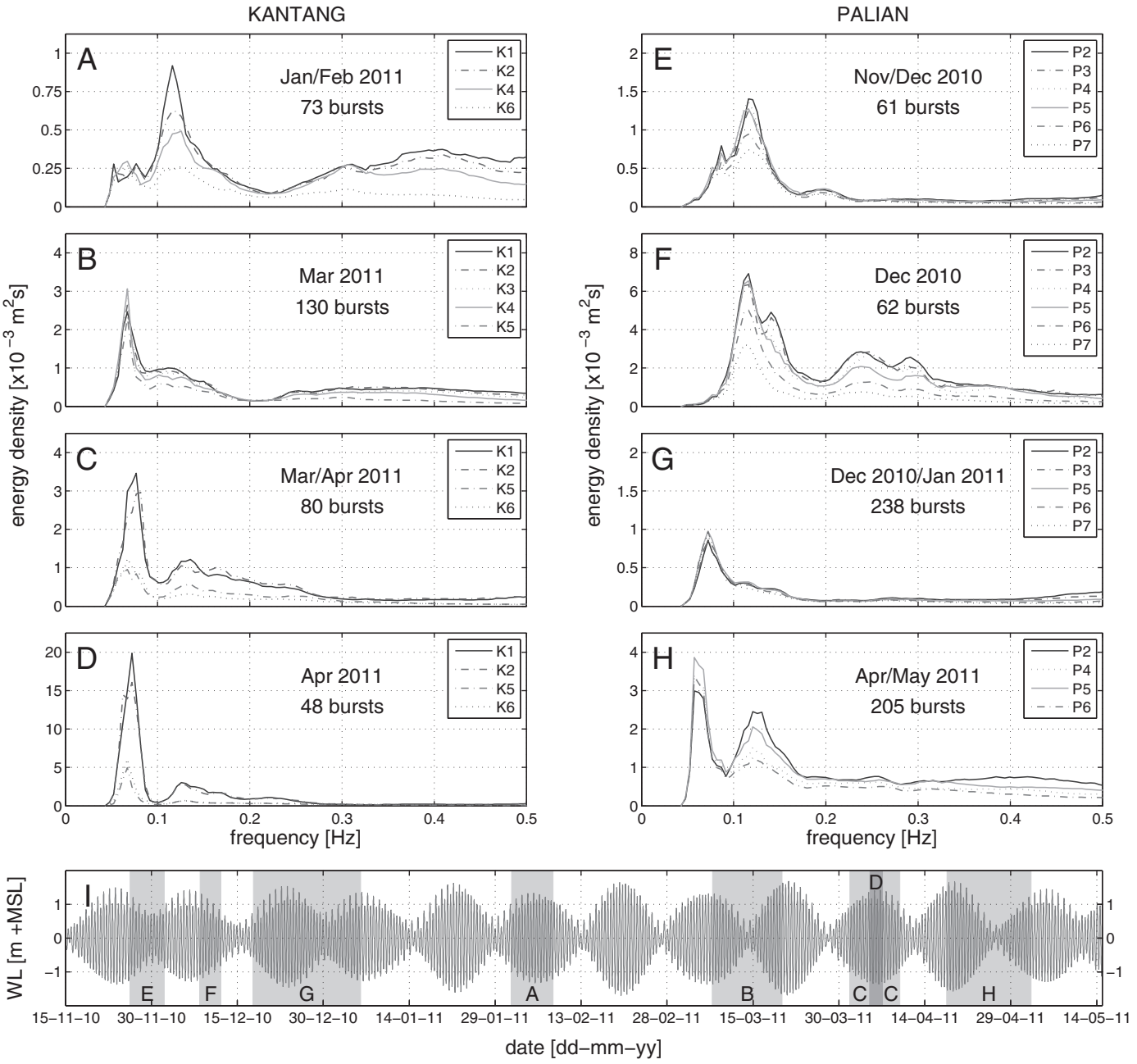

Fig. 5. Averaged wave energy density spectra of simultaneously obtained wave data during full inundation of the cross-shore transects (A–D) at Kantang and (E–H) at Palian, each for four different periods. (I) Tidal conditions during the field campaign. The shaded areas in panel I represent the data collection periods of the spectra in panels A–H. Sensor positions (K1–K6 and P2–P7) refer to the positions indicated in Fig. 2.

Due to the quadratic relation between wave height and wave energy, total wave energy decreased more pronouncedly along the transects than the wave heights. Along the Kantang transect 68–74% of the total incident energy (2.0–7.2 J/m^2) was dissipated over the 246 m stretch between the first and last sensor (Fig. 6C). During the March deployment, 53% of the incident energy (2.9 J/m^2) was attenuated between K1 and K5 (196 m apart). At Palian, 52–71% of the mean incident total wave energy (1.3–9.4 J/m^2) was attenuated between the first and last sensor, which were only 98 m apart (Fig. 6K). During the final data collection period, 41% of the incident energy (5.0 J/m^2) was attenuated between P2 and P6 (only 75 m apart).

Observed wave heights were ranging up to about 15% of the simultaneously measured water depths (Fig. 6D,L). Wave breaking occurs for wave heights exceeding 60–83% of the water depth (Battjes and Stive, 1985). Hence, wave breaking could not have contributed significantly to the wave energy losses along the transects. Therefore we conclude that the observed attenuation of wave energy must have been caused by drag and friction forces induced by the mangrove vegetation and interactions with the forest floor.

When severe storms hit the Kantang transect, only three wave sensors collected proper data. Wave data for March 27 and 28 (2011) are plotted in Fig. 7 (without selecting those bursts for which all three

sensors were inundated). Significant wave heights exceeded 30 cm during the most extreme conditions. Mean significant wave heights decreased from 15.3 cm to 6.5 cm (−58%) between K2 and K4 (Fig. 7A), which were 102 m apart and only had the sparsely vegetated forest fringe in between. Consequently, 81% of the incident wave energy (15.4 J/m^2) was attenuated between these two stations (Fig. 7C). As wave heights ranged up to 40% of the water depth (Fig. 7D), wave breaking was observed (visually), but still to a limited extent. Hence, even during storm conditions, the vegetation and bottom induced drag and friction forces were the major drivers for wave attenuation.

Within the first data series for the Kantang transect, average significant wave heights increase by 6% between K3 and K4 (Fig. 6A). Similarly, within the last data series for the Palian transect, an 11% increase of

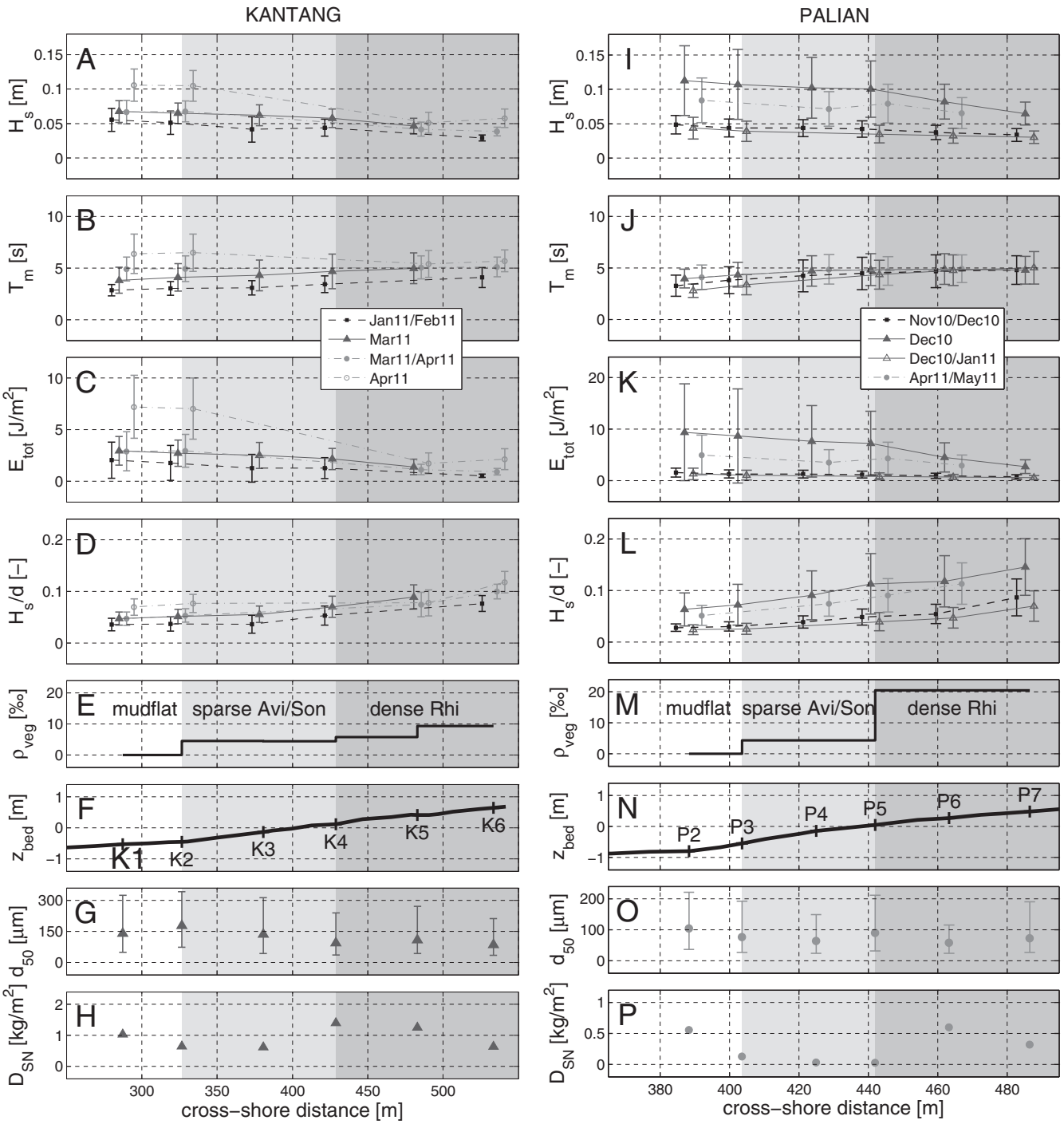

Fig. 6. Biogeophysical conditions along the transects: (A,I) significant wave heights H_s [m]; (B,J) mean wave periods T_m [s]; (C,K) total wave energy E_{tot} [J/m^2]; (D,L) wave heights divided by water depths H_s/d [−]; (E,M) vegetation densities ρ_{veg} within 1 m above the forest floor [volume-‰]; (F,N) elevation z_{bed} [m + MSL]; (G,O) mean grain size of the top soil layer d_{50} [µm] with error bars indicating d_{25} and d_{75}; and (H,P) net sediment deposition during a full spring–neap tidal cycle D_{SN} [kg/m^2], each for the Kantang and Palian transect, respectively. Plots of the wave characteristics present mean observed values, with error bars indicating the standard deviation. Data comprise four different periods for each transect. Note that horizontal offsets in the upper panels are just for visibility, monitoring positions were equal throughout all periods.

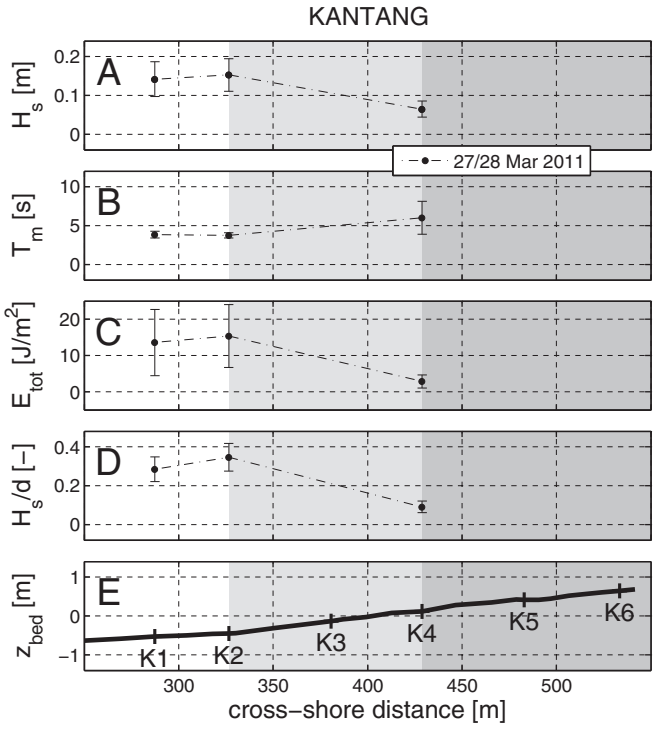

Fig. 7. Wave characteristics along the Kantang transect (same as Fig. 6) for a two-day storm period.

the average significant wave height is observed between P4 and P5 (Fig. 6I). These observations coincide with the sudden increase of the vegetation density just behind K4 and P5 (Fig. 6E,M), possibly causing wave reflection at the edge of the dense *Rhizophora* vegetation (cf. Massel et al., 1999; Méndez et al., 1999). During storm conditions, this same phenomenon is presumably observed in front of the sparse vegetation of the *Avicennia* zone at the Kantang transect, when the wave height shows a local increase of about 8% (Fig. 7A).

4.4. Sediment characteristics and cross-shore deposition patterns

The bed material at both transects consisted of a sandy mud, containing on average 34(±7)% (±standard deviation) and 45(±6)% silts (<63 μm) at the Kantang and Palian transect, respectively. The soils contained 10(±1)% and 10(±3)% organic material at the respective transects. At the Kantang transect, mean grain sizes (d_{50}) gradually fined towards the back of the forest, from 177 to 86 μm (Fig. 6G). At the Palian transect, fining of the sediments towards the back of the forest (105–58 μm) was interrupted at P5, where grain sizes were somewhat greater (90 μm) than those at the two seaward and landward monitoring positions (Fig. 6O). This local coarsening was in concordance with the slight increase in hydrodynamic activity observed around P5 (Fig. 6K). Sediment grain sizes of the soil samples taken from the top layer of the forest floor were generally coarser at positions with increased hydrodynamic activity (Fig. 8; Pearson's $R = 0.67$ ($p = 0.018$) for the correlation indicated by the fitted trend).

Net sediment deposition was correlated with the significant wave heights observed during the trapping experiments. For this comparison, we did not filter the wave data for concurrent observations along the entire transects. Deposition starts at the onset of flooding of any of the monitoring positions, so all wave dynamics (all bursts) at any location were included. Deposition rates observed during spring tide, for one tidal inundation at Kantang (0.05–0.26 kg/m^2) and for two tidal inundations at Palian (0.10–0.35 kg/m^2), did not show significant correlation with the observed significant wave heights (Fig. 9A). Notably, variations in the observed wave heights were really small these days.

Maximum deposition rates during a full spring–neap tidal cycle (~14 days) were only up to 5 times greater than those obtained during a single spring high tide, with deposition rates of 0.61–1.4 kg/m^2 and 0.03–0.60 kg/m^2 at Kantang and Palian, respectively (Fig. 6H,P). Overall, spring–neap tidal deposition rates rapidly reduced with a minor increase in mean observed significant wave heights (Fig. 9B; $R = -0.84$ ($p < 0.01$)). Along both transects, deposition rates decreased from the mudflat into the sparsely vegetated forest front (Fig. 6H,P). Further landward, in the dense *Rhizophora* vegetation, deposition rates suddenly increased, but then again decreased towards the back of the forest (Fig. 6H,P).

4.5. Linking wave attenuation to vegetation densities

Along with the decrease of wave height and energy along both transects, deviations around the mean observed values decreased into the forest (Fig. 6A,C,I,K): higher-than-average wave heights and energies were attenuated more effectively. With increasing wave heights (H) the relative amount of wave attenuation with respect to the total (incident) wave energy increases as wave energy dissipation due to vegetation scales with H^3 (Mendez and Losada, 2004), whereas wave energy scales with H^2. This phenomenon was as well demonstrated by the increased wave attenuation during storm conditions (Fig. 7A,C) with respect to regular conditions (Fig. 6A,C) along the Kantang transect.

For each transect, wave attenuation was analysed for the data collected during the first two deployments, spanning the first two data series for Kantang (Fig. 5A–B) and the first three data series for Palian (Fig. 5E–G). These series contained data for most monitoring positions along both transects. Wave attenuation was computed for each vegetation zone separately: mudflat, sparsely vegetated forest front, densely vegetated back forest. Per data burst, the decrease of the wave height for each zone ($\Delta H = H_{x1} - H_{x2}$ [m]) was standardized to the wave height loss per unit distance ($\Delta H / \Delta x$ [−]) by dividing with the distance between the front most monitoring position (x_1) and the last position (x_2) within any vegetation zone ($\Delta x = x_2 - x_1$ [m]).

Standardized wave attenuation correlated rather poorly with the incident wave heights at the mudflats with correlation coefficients (R) of 0.21 and 0.17 ($p < 0.01$) for the Kantang and Palian transect, respectively (Fig. 10A,D). Within the mangroves, this correlation strongly improved for increasing vegetation densities: correlation coefficients were

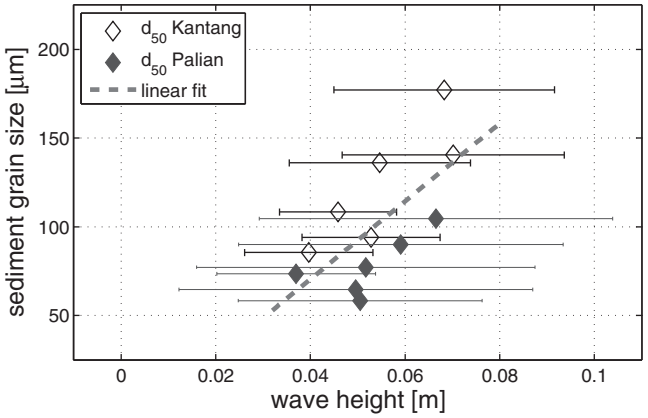

Fig. 8. Mean sediment grain sizes d_{50} [μm] along the transects versus the observed significant wave heights H_s [m]. Plotted error bars indicate means ± standard deviations of the observed wave heights during all measurement periods at each transect.

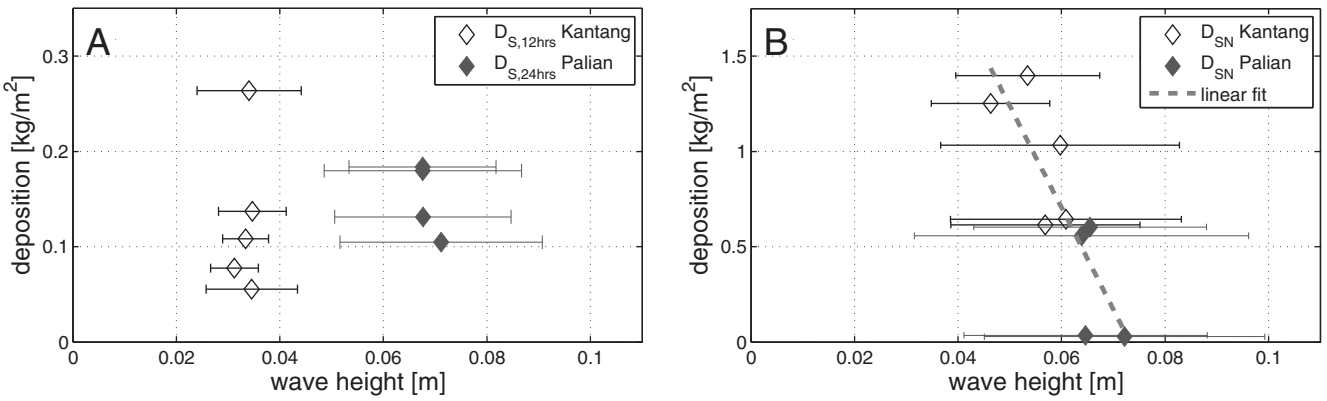

Fig. 9. Net sediment deposition rates [kg/m^2] observed (A) during one/two spring tidal cycles (12/24 h) at Kantang and Palian, respectively, and (B) during a full biweekly spring–neap tidal cycle, also at Kantang and Palian. Plotted error bars indicate means ± standard deviations of the significant wave heights H_s [m] during the respective sediment trapping periods.

0.52 and 0.58 ($p \ll 0.001$) in the *Avicennia* zones at Kantang and Palian, respectively (Fig. 10B,E), while they further increased to 0.66 and 0.91 ($p \ll 0.001$) for the *Rhizophora* zones of the respective transects (Fig. 10C,F).

According to previous work, the rate of wave attenuation per unit length in the direction of wave propagation is defined by (Mazda et al., 2006):

$$r = \frac{\Delta H}{H}\frac{1}{\Delta x} \tag{1}$$

wherein r [m^{-1}] is the wave attenuation rate and H represents the wave height at the sea side monitoring position (H_{x1}). Eq. (1) was rewritten into a derivative representing the linear increase of the wave attenuation for increasing incident wave heights:

$$r = \frac{d(\Delta H/\Delta x)}{dH}. \tag{2}$$

Accordingly, from the results in Fig. 10, generalized wave attenuation rates were obtained for all vegetation zones, each applying to a range of incident wave heights and water depths. These rates increased for the greater vegetation densities towards the back of both transects (Table 2). Consequently, the wave attenuation rates correlated

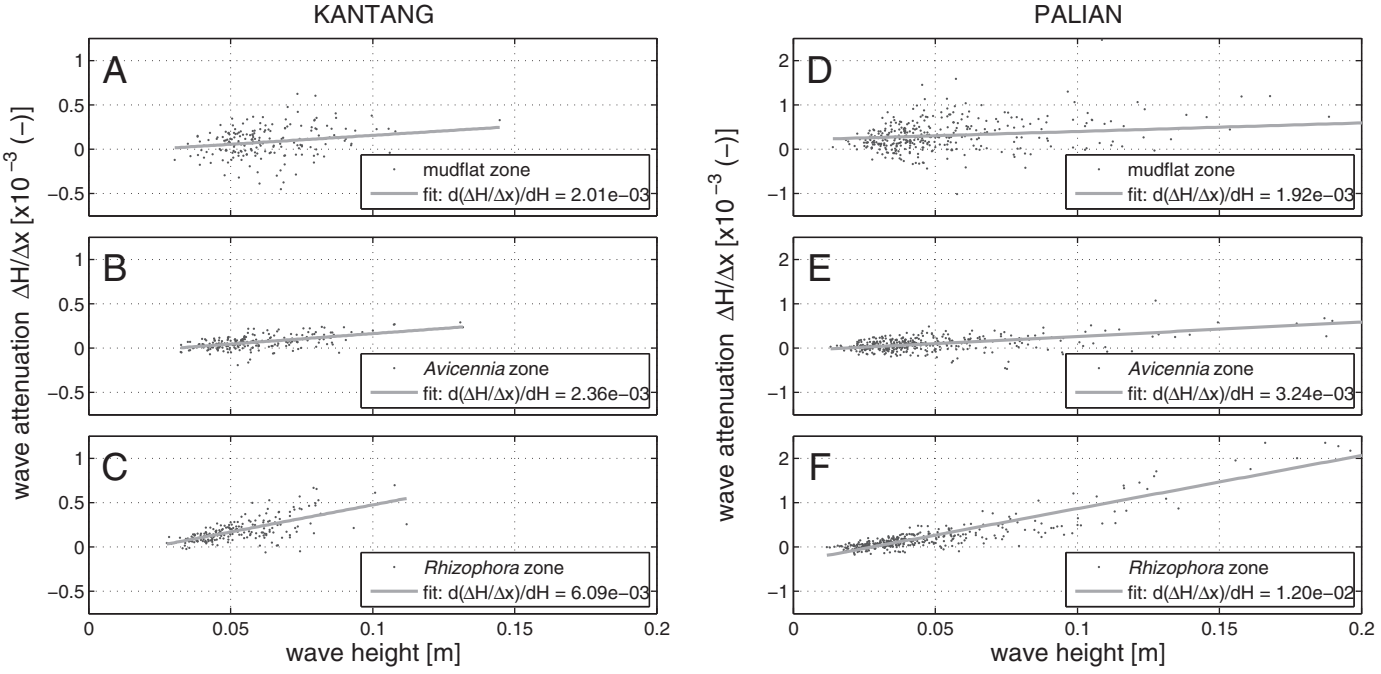

Fig. 10. Correlation between the incident significant wave height H_s [m] and the wave attenuation, expressed as wave height loss per unit distance $\Delta H/\Delta x$ [−]. Results comprise the respective vegetation zones: (A,D) mudflats, (B,E) sparsely vegetated *Avicennia*/*Sonneratia* zones at the forest front and (C,F) denser vegetated *Rhizophora* zones further inland, for the Kantang and Palian transects, respectively.

Table 2
Obtained wave attenuation rates r [m^{-1}] and calculated shoaling coefficients K_s [m^{-1}], both per unit distance.

	Kantang		Palian	
	r [m^{-1}]	$1 - K_s$ [m^{-1}]	r [m^{-1}]	$1 - K_s$ [m^{-1}]
Mudflats	$2.0 \cdot 10^{-3}$	$1.0 \cdot 10^{-4}$	$1.9 \cdot 10^{-3}$	$2.7 \cdot 10^{-3}$
Avicennia zones	$2.4 \cdot 10^{-3}$	$-4.9 \cdot 10^{-4}$	$3.2 \cdot 10^{-3}$	$-9.9 \cdot 10^{-4}$
Rhizophora zones	$6.1 \cdot 10^{-3}$	$-1.6 \cdot 10^{-3}$	$1.2 \cdot 10^{-2}$	$-3.1 \cdot 10^{-3}$

significantly with the volumetric vegetation densities within 1 m above the forest floor ($R = 0.98$ ($p < 0.001$); Fig. 11A). The best fit of the wave attenuation rate with respect to the vegetation density (ρ_{veg}) in volume-‰ resulted in the following expression:

$$r = 5.1 \cdot 10^{-4} \cdot \rho_{veg} + 1.5 \cdot 10^{-3}. \quad (3)$$

This expression quantifies the incline of the attenuating capacity of mangrove vegetation with increasing vegetation densities. Roughly, the generalized attenuation rate increases by about 0.005 m^{-1} with a 10‰ increase of the volumetric vegetation density within 1 m above the forest floor. A similar result is obtained if wave heights H in Eqs. (1) and (2) are substituted with the wave energy E. The obtained wave energy attenuation rate r_E [m^{-1}] correlates with the vegetation density according to the following expression ($R = 0.97$ ($p = 0.001$); Fig. 11B):

$$r_E = 6.9 \cdot 10^{-4} \cdot \rho_{veg} + 2.8 \cdot 10^{-3}. \quad (4)$$

Obviously, on the mudflats, where no vegetation was present, waves were attenuated by the shallow water interactions with the bottom. The observed positive wave attenuation rate at zero vegetation density in Fig. 11A, represented by the offset of Eq. (3), is induced by the bottom friction and possibly (no observational evidence) by viscous dissipation over the cohesive soft mud (Elgar and Raubenheimer, 2008; Winterwerp et al., 2007). Viscous dissipation is expected to reduce inside the forest due to the enhanced consolidation of the substrate through water extraction by and growth of the subsurface root systems of the mangroves (Augustinus, 1995). Nevertheless, wave attenuation rapidly increases for increasing vegetation densities and, consequently, the wave attenuation within the forest is rapidly dominated by vegetation induced drag forces (Fig. 11).

Alternatively, wave height attenuation was computed for each individual data burst directly from Eq. (1). Concurrent volumetric vegetation volumes within the water column were obtained for every single burst by integrating the relative volume of vegetation elements below the average water level between any pair of monitoring positions. Consequently, a much greater range of vegetation densities was obtained than those plotted in Fig. 11, as the volumetric vegetation densities varied with the water depth (cf. Fig. 4A). Accordingly, a range of wave attenuation rates was obtained from the individual data bursts (Fig. 12).

At the Kantang transect, single-burst attenuation rates r ranged from about 0.001 m^{-1} in the *Avicennia* zone, to values increasing from 0.002 m^{-1} to 0.005 m^{-1} in the *Rhizophora* zone (Fig. 12A). Variations in the vegetation density within the *Avicennia* zone were rather small, hence no real variation in the wave reduction was obtained. At the Palian transect, within the *Avicennia* zone again no real variation in the wave attenuation ($r = 0.002$ m^{-1}) was obtained. However, variability of the vegetation densities in the dense *Rhizophora* zone was substantial and wave attenuation increased from 0.001 to 0.007 m^{-1} for an increase of the vegetation density from 19‰ to 32‰ (Fig. 12B).

Due to the decrease of vegetation densities at increasing elevations (Fig. 4), greater water depths induced decreasing vegetation densities and, consequently, reduced wave attenuation rates (Fig. 13). Due to the limited vertical variability of the vegetation structure in the *Avicennia* zones once the pneumatophores were flooded (Fig. 4A), wave attenuation rates were rather independent of the water depth ($r = 0.001$–0.002 m^{-1}; Fig. 13A,B). The slight increase of wave attenuation rates in these zones could have been caused by submergence of the canopy of the lower trees at the highest tides. Conversely, the gradual decrease of the number of roots with increasing elevations in the *Rhizophora* zones caused the wave attenuation to drop progressively for increasing water depths ($r = 0.006$ m^{-1} to $r = 0.001$–0.002 m^{-1}; Fig. 13A,B). Consequently, contrary to the absence of a correlation between incident wave heights and water depths at K1 and P2, in the back of the forest wave heights and water depths become correlated ($R = 0.67$ ($p \ll 0.001$) and $R = 0.30$ ($p \ll 0.001$) at K6 and P7, respectively).

5. Discussion

5.1. Effects of different vegetation characteristics

In a previous study, Brinkman (2006) observed reductions of total wave energy at three different mangrove sites (Cocoa, Oonoonba, Iriomote) of 64%, 95% and 71% along transects of respectively 260 m, 40 m and 40 m in length. Along with these findings, significant wave heights were found to decrease by 50%, 75% and 54% along the respective transects (Table 1). The latter two reduction rates of both wave energy and height are quite high compared to the energy reduction (41–74%; Fig. 6C,K) and wave height attenuation (22–47%; Fig. 6A,I) obtained in the present work. Nevertheless, obtained wave attenuation rates ($r =$

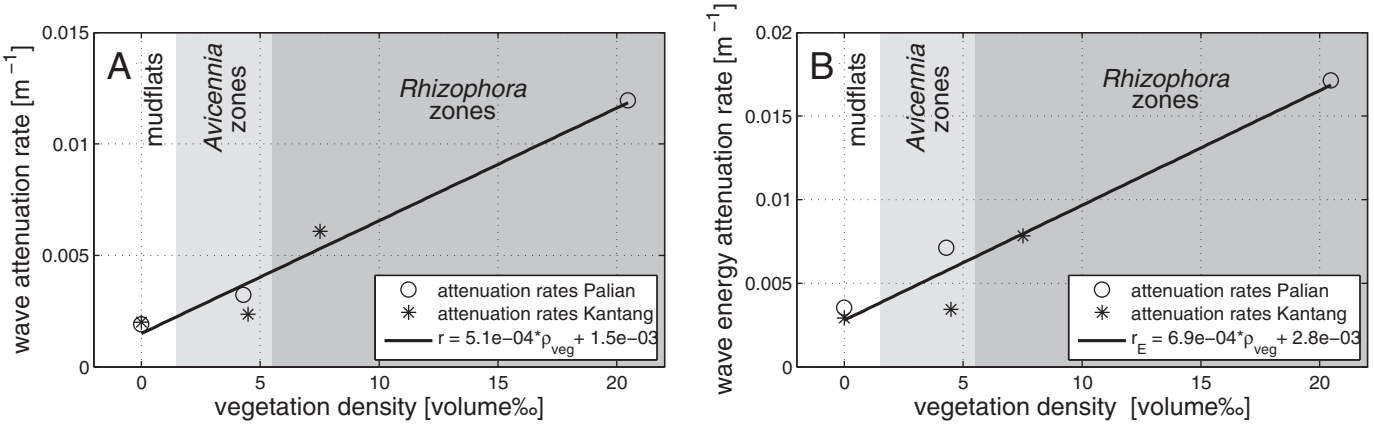

Fig. 11. Attenuation rates of (A) wave heights r [m^{-1}] and (B) wave energy r_E [m^{-1}] for the characteristic vegetation zones at each transect correlate significantly with the volumetric vegetation density within 1 m above the forest floor ρ_{veg} [‰].

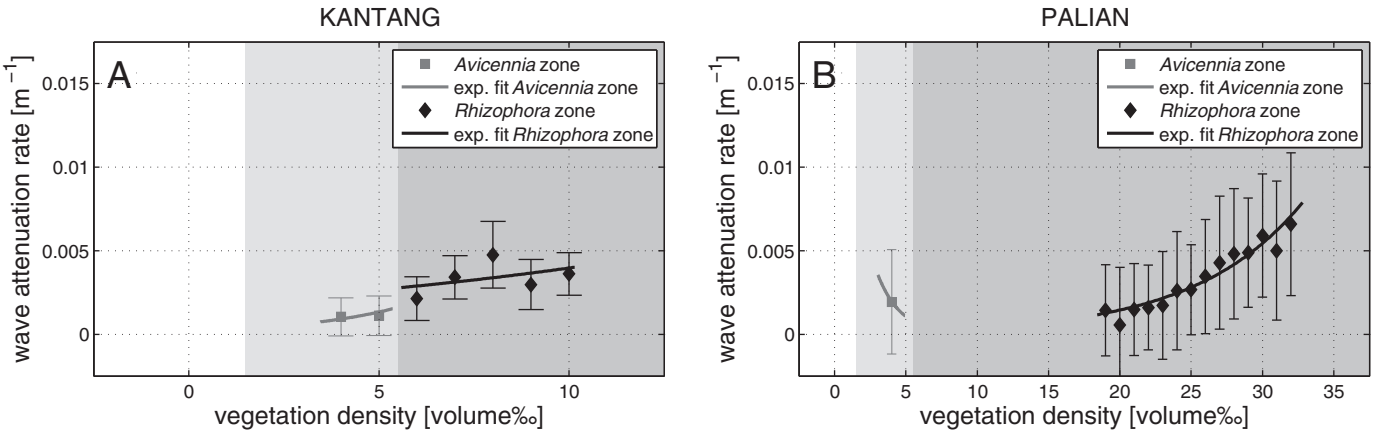

Fig. 12. Wave attenuation rates r [m^{-1}] increase with the relative volume of submerged vegetation ρ_{veg} [volume‰] at (A) the Kantang transect and (B) the Palian transect (error bars indicate mean ± the standard deviation).

0.002–0.012 m^{-1}; Fig. 11) compare well with previous observations by e.g. Mazda et al. (2006) for a transect along the Vinh Quang coast, Vietnam: 0.001–0.004 m^{-1}; and Quartel et al. (2007) at their Red River site: 0.004–0.012 m^{-1} (Table 1).

At the same time, Quartel et al. (2007) obtained increasing wave attenuation rates for increasing water depths within the mangroves, while Mazda et al. (1997a) found the wave attenuation to be rather constant with variable water depths. These findings are in contrast with the significant decrease of the wave attenuation with increasing water depth observed in the present study, in particular in the dense *Rhizophora* vegetation (Fig. 13). This contrasting behaviour is instigated by the limited height of the dwarfed trees in the field sites of the former studies, while vegetation in the present study was highly developed with trees up to about 20 m high.

The variability in previously and currently obtained wave attenuation data underlines the susceptibility of mangroves' attenuating capacity to variations in both hydrodynamic forcing (incident wave energy, water depth) and vegetation characteristics. Consequently, detailed information on both hydrodynamic conditions and vegetation characteristics is imperative for a mechanistic understanding of the vegetation induced wave attenuation in mangroves. Rough vegetation parameters, such as the number of trees, tree height and leaf cover (e.g. Bao, 2011; Quartel et al., 2007) are inadequate for developing explicit relations for the wave attenuation in mangroves of arbitrary constituency (in terms of species composition and tree structure) under variable hydrodynamic conditions. Instead, the volume of submerged vegetation, as adopted in the present study, is a comprehensive characterization of the vegetation structure (Mazda et al., 1997b), facilitating the development of such generic relations (sensu Eqs. (3) and (4)).

5.2. Physical processes affecting wave propagation in mangroves

Wave data presented in this paper were collected with robust, autonomous pressure gauges. Comparison of the water depths obtained simultaneously with high-frequency wave sensors (MacroWave) and low-frequency pressure loggers (Sensus Ultra) rendered near-unity correlations. This finding confirms the accuracy of the data retrieved with the wave sensors for the water depths observed in the field. The resolution of the wave sensors was ~0.7 cm (0.01 psi), limiting the detection of waves of a few centimetres in height (<1–3 cm; Fig. 10). The few negative wave attenuation values in Fig. 10 could be due to the limited resolution of the equipment. However, no proof was found for structural errors in the obtained wave data and these negative attenuation values could also be induced by local wind effects (mainly in front of the forest) or wave reflection.

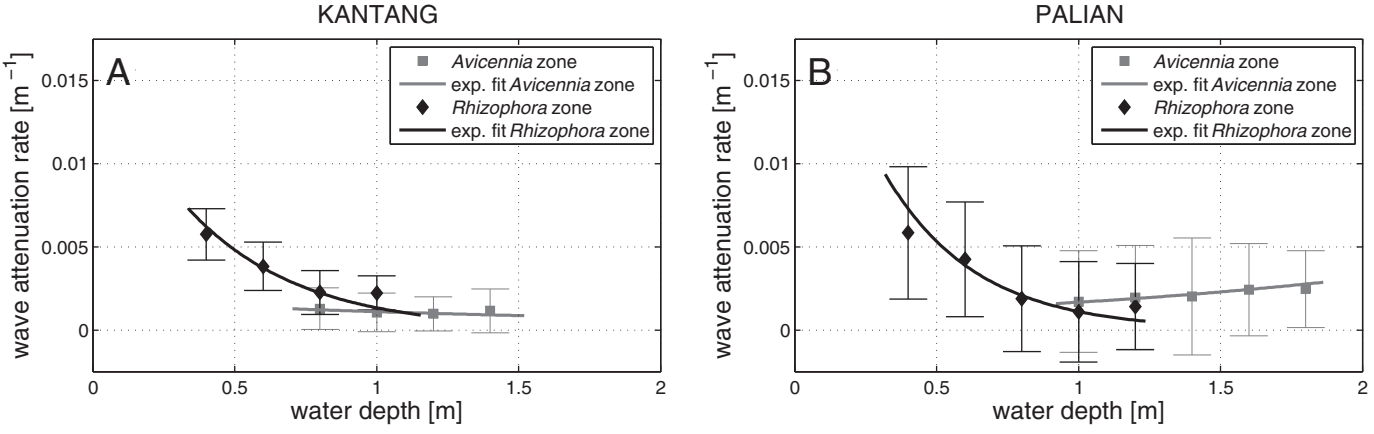

Fig. 13. Wave attenuation rates r [m^{-1}] correlate with the concurrent water depths [m] at (A) the Kantang transect and (B) the Palian transect (error bars indicate mean ± the standard deviation).

Sudden cross-shore changes in the vegetation density might have induced locally increasing wave heights due to wave reflection (Massel et al., 1999; Méndez et al., 1999). This was noted in some of the data collected at the transition from the sparsely vegetated *Avicennia* zone to the much denser *Rhizophora* vegetation at both transects (Fig. 6A,I). The observed wave reflection (6–11%) is similar to the 0.07 reflection coefficient computed by Massel et al. (1999) for an artificial mangrove fringe. For severe wave conditions during a storm period, wave heights even showed a minor increase (8%) at the relatively sparse vegetation fringe of the *Avicennia* zone at the Kantang transect (Fig. 7A). Hence, along with the increasing attenuating capacity of mangrove vegetation (Fig. 10), wave reflection might increase for higher incident waves. The latter is similar to the enhanced reflection of higher waves at submerged permeable structures (Ting et al., 2004).

Wave shoaling also causes wave heights to increase in shallow coastal waters (Van Rijn, 2008). Shoaling coefficients computed from the observed water depths and wave characteristics, assuming linear wave theory, range between 1.00049 and 1.0031 per unit distance. When subtracting the shoaling coefficient from unit value, the rate of change of the wave height due to shoaling is obtained, allowing easy comparison with the measured wave reduction rates (Table 2). The resulting negative shoaling rates identify increasing wave heights within each of the vegetated zones. Shoaling rates are greater for the steeper slopes of the Palian transect (Fig. 2). The computed increase of the wave heights due to shoaling is about 20–30% of the measured wave reduction within the mangrove vegetation (Table 2). Consequently, gross attenuation of wave heights by the mangrove vegetation is expected to be 20–30% greater than the presented (total) wave attenuation rates.

Obtained shoaling rates are up to an order of magnitude smaller than the attenuation rates (Table 2). As the shoaling and attenuation rates were computed with the significant wave heights, they should (approximately) apply to the spectral peaks in the wave energy density spectra presented in Fig. 5. Consequently, we argue that the increase of the spectral peaks in the swell regime observed during some of the deployments (Fig. 5B,G,H) was mainly induced by wave energy transfer to lower frequencies due to nonlinear wave–wave interactions (cf. Elgar and Raubenheimer, 2008) and not by shoaling.

This paper focusses on the net contribution of mangrove ecosystems to wave attenuation. The mangrove ecosystem includes the smoothly sloping muddy forest floor, causing an increase of wave heights due to shoaling and enhancing wave reduction through bed roughness and (possibly) viscous dissipation. Quantifying the exact contribution of vegetation induced drag forces, shoaling, bottom friction and viscous dissipation to the observed attenuation rates was impossible for the presented field data. The effects of these different processes on e.g. the wave period and wave energy flux could not be isolated from the field data. In addition, one should take into account the effects of percolation: the loss of energy due to water exchange with the bed in response to the pressure gradient underneath waves (Möller et al., 1999). The present study unifies all these effects in a total wave attenuation rate, similar to previous studies that presented bulk friction factors representing all or most wave modulating processes (Paul and Amos, 2011; Quartel et al., 2007).

Nevertheless, we argue that energy losses due to vegetation drag dominated the energy losses due to bottom friction or viscous dissipation as the attenuation rates were smallest on the bare mudflats and significantly increased inside the mangrove vegetation (Fig. 11). Inside the forest, very high near-bed vegetation densities prevent exposure of the forest floor (Fig. 4A).

5.3. Physical processes determining sedimentation in mangroves

The results of this study also address the contribution of fringing mangroves to sediment trapping. Whereas sedimentation in mangroves is supposedly governed by the trapping of sediments that are imported by tidal dynamics, erosion is generally due to surface waves (Winterwerp et al., 2013). Along with the wave data, we also collected tidal flow data during the March measurements at Kantang and during the April/May data collection at Palian (Horstman et al., 2013). With the observed wave characteristics during these periods, time-averaged near-bed peak orbital velocities ranged between 7 and 13 cm/s (assuming linear waves), whereas time-averaged tidal flow velocities were about 5 cm/s on the mudflats and rapidly reduced to only a few cm/s inside the vegetation (Horstman et al., 2013; Figs. 7 and 8). Consequently, time-averaged bed shear stresses due to waves ($O(1)$ N/m^2) are two orders of magnitude greater than those due to the tidal current ($O(10^{-2})$ N/m^2). Hence, although the tides bring in the sediments, the dominant bed shear stresses due to the waves are limiting the sediment deposition.

Observed sediment characteristics and bi-weekly deposition rates were indeed found to correlate inversely with the wave exposure of the mangrove sites (Figs. 8, 9). Reduction of the wave energy by mangroves facilitates the trapping of sediments (Van Santen et al., 2007; Winterwerp et al., 2013). Cross-shore increases in vegetation density, giving rise to increased wave attenuation, allow for the progressive deposition and trapping of finer materials. This was confirmed by the gradual decrease of the mean grain size of the bed material along the studied transects (Fig. 6G,O). Consequently, in the shelter of the dense *Rhizophora* trees, allowing for the deposition of finer sediment fractions, deposition suddenly increased (Fig. 6H,P). Additionally, increases of the wave energy, for instance due to wave reflection, locally reduced deposition rates while a local coarsening of the bed material was observed (Fig. 6O,P).

5.4. Quantifying bio-physical interactions in mangroves

To further study the bio-physical interactions in mangroves and to quantify the contribution by particular mangrove characteristics (e.g. vegetation characteristics, bed roughness and bed slope) to their attenuating capacity, mechanistic modelling studies are required. In contrary to the presented field observations, physical and numerical modelling allow for controlled observations and simulations of those processes contributing to the total wave attenuation rate in mangrove forests: vegetation induced drag forces, bottom friction, viscous dissipation and shoaling. Understanding the contribution by any of these processes is key to future investigations of the capacities and limitations of any arbitrary mangrove forest to attenuate wave energy and to trap sediments. Detailed and integrated field observations of the vegetation, hydrodynamics and morphology of characteristic mangrove systems, as presented (for the first time) in this paper, provide crucial input to these mechanistic studies.

6. Conclusions

This paper presented field observations of wave attenuation and sediment dynamics along two cross-shore transects in coastal mangroves in Southern Thailand. Collection of wave data in combination with detailed vegetation measurements was unprecedented, but is of great importance to the further development of knowledge on the attenuation of waves in mangrove vegetation.

The detailed characterization of the vegetation cover at the field sites emphasizes the variability of mangrove vegetation structure in both the vertical and the horizontal direction. Vegetation densities were strongly dependent of the dominant vegetation type. Volumetric vegetation densities within 1 m above the forest floor were found to be 4.3–4.5‰ in the *Avicennia* zones along both transects. Vegetation densities in the *Rhizophora* zones were (much) higher: 5.8–9.3‰ at the Kantang transect and 20‰ at the Palian transect, increasing up to 32‰ for water depths less than 1 m.

Mean observed significant wave heights decreased (on average) by 42–47% along the Kantang transect, which was 246 m long, and with

30–43% along the Palian transect, which was only 98 m long. Along the same transects, total wave energy (on average) decreased with 68–74% and 52–71%, respectively. For increased wave heights during storm conditions, we observed a maximum wave energy reduction of 79% over 141 m, while significant wave heights were reduced up to 54%. Wave attenuation was most efficient for short sea waves (<10 s), while swell waves (10–20 s) tended to maintain their energy or even gained energy by the attenuation of the shorter waves.

Wave attenuation was also found to correlate positively with the incident wave height. The generalized total wave attenuation rates, obtained by the gradient of the relation between wave height reduction and incident wave height for each of the different vegetation zones, ranged between 0.002 and 0.012 m^{-1}. These rates showed a significant positive correlation with the volumetric vegetation density. Presented total wave attenuation rates comprise effects of shoaling and energy losses due to various bio-physical interactions within the mangrove ecosystem. We argue that the observed wave attenuation in the mangroves is dominated by energy losses due to vegetation drag. Energy losses due to bottom friction and viscous dissipation on the bare mudflats induce attenuation rates that are significantly lower than those inside the mangrove vegetation.

Reductions of the wave energy by the mangroves were found to facilitate greater bi-weekly net deposition rates along both transects. Reduced hydrodynamic activity towards the denser vegetated back of the mangrove forests allowed for the deposition of finer sediments, as confirmed by the gradual fining of the bed material. A local reduction of the deposition rate and increase of the mean grain size were observed at the interface between the sparsely vegetated forest fringe and the dense *Rhizophora* vegetation, where wave reflection supposedly gave rise to a local increase of the wave energy.

These findings emphasize the coastal defence function of mangroves and provide a starting point for mechanistic modelling studies to investigate the processes contributing to the attenuating and sediment trapping capacity of mangroves.

Acknowledgements

The authors gratefully acknowledge all assistance in planning, facilitating and executing fieldwork by T. Balke, D. Galli, D.A. Friess, E.L. Webb, C. Sudtongkong, Katai, Dumrong and Siron. We also thank T.J. Bouma, C.J.L. Jeuken, T. Balke, D.S. van Maren, P.M.J. Herman and J.M. Hendriks for the fruitful discussions during the preparations of the fieldwork and this paper. We acknowledge L. van IJzerloo for the sediment analysis. Two anonymous reviewers have helped to improve this paper with their constructive comments.

Fieldwork presented in this paper was conducted under the research permit 'Ecology and Hydrodynamics of Mangroves' granted by the National Research Council of Thailand (Project ID-2565) and funded by the Singapore-Delft Water Alliance's mangrove research programme (R-264-001-024-414).

Appendix A. Spectral analysis

For the spectral analysis of the obtained water level time series we followed the six-step method presented by Hegge and Masselink (1996):

1. De-trending the signal to overcome within-burst tidal water level fluctuations.
2. Applying a Hann-taper *w* for preventing leakage of spectral density from large peaks:

$$w(n) = 0.5\left(1 - \cos\frac{2\cdot\pi\cdot n}{N-1}\right) \quad for\ \ n = 1, 2\ldots, N \tag{A.1}$$

wherein *N* is the length of the data series (i.e. 4096).

3. Running an FFT procedure to calculate the Fourier coefficients $X(m)$ of the observed water depth time series $x(n)$ of length *N*. Each coefficient relates to a frequency interval $f(m)$:

$$X(m) = \sum_{n=1}^{N} x(n)\cdot e^{-2\pi i(m-1)(n-1)/N} \quad for\ \ m = 1, \ldots, N \tag{A.2}$$

$$f(m) = m\cdot f_s/N \quad for\ \ m = 1, \ldots, N. \tag{A.3}$$

With f_s representing the sampling frequency (i.e. 10 Hz).

4. Calculating the pressure response factor K_p in order to take into account the attenuation of the wave signal towards the bed. This factor depends on the water depth and wave length and hence can only be calculated after the FFT has been executed. Assuming linear wave theory K_p [−] can be calculated as (CERC, 1984):

$$K_p(m) = \frac{\cosh(k(m)\cdot z)}{\cosh(k(m)\cdot d)} \quad for\ \ m = 1, \ldots, N. \tag{A.4}$$

With the wave number $k = 2\pi / L$ [m^{-1}] calculated for each frequency interval $f(m)$ of the Fourier coefficients. The water depth *d* [m] and the elevation of the sensor above the bed *z* [m] are assumed constant within each burst.

5. Calculating the one-sided periodogram P [m^2 s], expressing the spectral density as a function of the wave frequency in interval m. The one-sided periodogram follows from the Fourier coefficients. Only the first half ($1 \le N \le (N/2 + 1)$) of the Fourier coefficients is taken into account, as the second half consists of complex conjugates:

$$\begin{aligned} P(m) &= \frac{\left|X(m)\cdot K_p(m)^{-1}\right|^2}{f_s N} \quad for\, m = 1, \frac{N}{2}+1 \\ P(m) &= \frac{2\cdot\left|X(m)\cdot K_p(m)^{-1}\right|^2}{f_s N} for\, m = 2, \ldots, \frac{N}{2}. \end{aligned} \tag{A.5}$$

6. Applying a correction factor *C* to take into account the effect of the taper in step 2 and calculating the energy density spectrum *S*:

$$C = \frac{N}{\sum_{n=1}^{N} w(n)^2} \tag{A.6}$$

$$S(f(m)) = C\cdot P(m) \quad with\ \ m = 1, \ldots, N/2. \tag{A.7}$$

With $f(m)$ the frequency [Hz] of the *m*th component of the energy density spectrum *S* [m^2 s].

The results of this procedure were used to derive significant wave heights (H_s [m]), root-mean-square wave heights (H_{rms} [m]), mean wave periods (T_m [s]) and total wave energy (E_{tot} [J/m^2]) for every burst of wave data:

$$E_{tot} = \sum_{m=1}^{N/2} S(f_m)\cdot\Delta f\cdot\rho g \tag{A.8}$$

$$H_s = 4\sqrt{m_0} \tag{A.9}$$

$$H_{rms} = 2\sqrt{2\cdot m_0} \tag{A.10}$$

$$T_m = m_0/m_1 \tag{A.11}$$

wherein Δf represents the frequency bandwidth of the spectrum (i.e. f_s/N [Hz]) and m_0 and m_1 are the 0th and 1st spectral moments of the energy density spectrum:

$$m_a = \sum_{m=1}^{N/2} S(f_m)\cdot {f_m}^a\cdot\Delta f \quad with\ \ a = 0, 1. \tag{A.12}$$

Appendix B. Vegetation data

B.1 Vegetation parameters transect Kantang

Table B.1
Vegetation composition and structure of the vegetation zones mapped along the Kantang transect (Fig. 2). For each tree type, the number N of individuals in a 20 × 20 m^2 survey plot is indicated, along with the diameter d [mm] of the tree trunk at multiple elevations z [m] above the forest floor. For the stilt root networks of *Rhizophora* trees, the number n and average diameter d [mm] of all elements are presented. For the pneumatophore cover of the forest floor, the number of pneumatophores N in three different 1 × 1 m^2 survey plots is presented, along with the average height h [mm] and diameter d [mm] of the pneumatophores in each plot.

Vegetation type	Category	TKI[a]						TKI[b]						TKII[a]						TKII[b]					
				$d(z)$						$d(z)$ or $n(z)$ $d(z)$						$d(z)$ or $n(z)$ $d(z)$						$d(z)$ or $n(z)$ $d(z)$			
		N	h; d	0.1 m	0.5 m	1.0 m	2.0 m	N	h; d	0.1 m	0.5 m	1.0 m	2.0 m	N	h; d	0.1 m	0.5 m	1.0 m	2.0 m	N	h; d	0.1 m	0.5 m	1.0 m	2.0 m
Pneumatophores[1]	S	392	50; 4.8	–	–	–	–	312	55; 6.6	–	–	–	–	28	37; 5.2	–	–	–	–	0	–	–	–	–	–
	M	724	44; 4.5	–	–	–	–	452	35; 5.5	–	–	–	–	213	36; 5.2	–	–	–	–	39	14; 5.7	–	–	–	–
	L	2172	82; 5.5	–	–	–	–	588	62; 6.0	–	–	–	–	519	46; 4.5	–	–	–	–	107	24; 6.9	–	–	–	–
Avicennia/*Sonneratia*[2]	XS	78	–	7	6	2	–	55	–	9	5	3	–	0	–	–	–	–	–	0	–	–	–	–	–
	S	70	–	23	17	13	–	35	–	22	17	14	–	0	–	–	–	–	–	0	–	–	–	–	–
	M	31	–	65	60	45	38	27	–	86	75	71	64	0	–	–	–	–	–	1		71	67	57	57
	L	9	–	170	130	122	104	9	–	230	210	200	169	0	–	–	–	–	–	0	–	–	–	–	–
	XL	2	–	1220	1190	1140	975	3	–	722	610	550	520	1	–	460	390	370	340	0	–	–	–	–	–
Rhizophora[3]	S	0	–	–	–	–	–	0	–	–	–	–	–	5	–	15 40	7 50	4 53	2 48	12	–	7 23	4 32	1 49	1 41
	M	0	–	–	–	–	–	6	–	11 22	17 18	7 18	10 8	14	–	310 27	115 23	50 30	13 47	36	–	168 23	76 24	42 24	9 36
	L	0	–	–	–	–	–	0	–	–	–	–	–	5	–	325 26	203 23	68 31	6 67	12	–	342 26	100 31	21 45	2 155
Dead stems[2]		0	–	–	–	–	–	9	610; 165	–	–	–	–	0	–	–	–	–	–	0	–	–	–	–	–

[1] Pneumatophore counts (N) are per plot of 1 m^2. Spatial coverage by the sparse (S), average (M) and dense (L) pneumatophore densities are assumed 20–60–20%, respectively.
[2] Tree counts (N) are per plot of 400 m^2. The *Avicennia* and *Sonneratia* trees are categorized according to their stem diameter (at breast height): 0–10 mm (XS), 10–25 mm (S), 25–100 mm (M), 100–200 mm (L) and >200 mm (XL).
[3] Tree counts (N) are per plot of 400 m^2. For the *Rhizophora* trees the total number of trees within each plot is assumed to consist of 20% smallest trees (S), 60% average trees (M) and 20% largest trees (L).

B.2. Vegetation parameters transect Palian

Table B.2
Vegetation composition and structure of the vegetation zones mapped along the Palian transect (Fig. 2). For each tree type, the number N of individuals in a 20 × 20 m^2 survey plot is indicated, along with the diameter d [mm] of the tree trunk at multiple elevations z [m] above the forest floor. For the stilt root networks of *Rhizophora* trees, the number n and average diameter d [mm] of all elements are presented. For the pneumatophore cover of the forest floor, the number of pneumatophores N in three different 1 × 1 m^2 survey plots is presented, along with the average height h [mm] and diameter d [mm] of the pneumatophores in each plot.

Vegetation type	Category	TPI						TPII					
				$d(z)$						$d(z)$ or $n(z)$ $d(z)$			
		N	h; d	0.1 m	0.5 m	1.0 m	2.0 m	N	h; d	0.1 m	0.5 m	1.0 m	2.0 m
Pneumatophores[1]	S	460	35; 5.0	–	–	–	–	–	–	–	–	–	–
	M	516	43; 5.6	–	–	–	–	–	–	–	–	–	–
	L	1728	50; 4.5	–	–	–	–	–	–	–	–	–	–
Avicennia/*Sonneratia*[2]	XS	1	–	16	10	–	–	290	–	24	9	8	–
	S	0	–	–	–	–	–	2	–	56	44	40	S
	M	0	–	–	–	–	–	5	–	69	55	58	51
	L	0	–	–	–	–	–	0	–	–	–	–	–
	XL	3	–	870	760	660	610	2	–	750	575	490	450
Rhizophora[3]	S	0	–	–	–	–	–	21	–	19 40	5 39	1 60	1 51
	M	0	–	–	–	–	–	61	–	191 28	72 25	24 38	8 22
	L	0	–	–	–	–	–	21	–	458 29	76 36	18 50	39 18

[1] Pneumatophore counts (N) are per plot of 1 m^2. Spatial coverage by the sparse (S), average (M) and dense (L) pneumatophore densities are assumed 20–60–20%, respectively.
[2] Tree counts (N) are per plot of 400 m^2. The *Avicennia* and *Sonneratia* trees are categorized according to their stem diameter (at breast height): 0–10 mm (XS), 10–25 mm (S), 25–100 mm (M), 100–200 mm (L) and >200 mm (XL).
[3] Tree counts (*N*) are per plot of 400 m^2. For the *Rhizophora* trees the total number of trees within each plot is assumed to consist of 20% smallest trees (S), 60% average trees (M) and 20% largest trees (L).

References

Alongi, D.M., 2008. Mangrove forests: resilience, protection from tsunamis, and responses to global climate change. Estuar. Coast. Shelf Sci. 76, 1–13.

Alongi, D.M., 2009. The Energetics of Mangrove Forests. Springer, Netherlands.

Anthony, E.J., 2004. Sediment dynamics and morphological stability of estuarine mangrove swamps in Sherbro Bay, West Africa. Mar. Geol. 208, 207–224.

Augustinus, P.G.E.F., 1995. Geomorphology and sedimentology of mangroves. In: Perillo, G.M.E. (Ed.), Developments in Sedimentology. Elsevier, pp. 333–357.

Bao, T.Q., 2011. Effect of mangrove forest structures on wave attenuation in coastal Vietnam. Oceanologia 53, 807–818.

Battjes, J.A., Stive, M.J.F., 1985. Calibration and verification of a dissipation model for random breaking waves. Journal of Geophysical Research: Oceans 90, 9159–9167.

Brinkman, R.M., 2006. Wave attenuation in mangrove forests: an investigation through field and theoretical studies. PhD Thesis James Cook University, Townsville, Australia, (146 pp).

Brinkman, R.M., Massel, S.R., Ridd, P.V., Furukawa, K., 1997. Surface wave attenuation in mangrove forests. Pacific Coasts and Ports '97, Christchurch, New Zealand, pp. 941–946.

CERC, 1984. Shore Protection Manual. U.S. Army Corps of Engineers, Washington DC.

Danielsen, F., et al., 2005. The Asian tsunami: a protective role for coastal vegetation. Science 310, 643.

Elgar, S., Raubenheimer, B., 2008. Wave dissipation by muddy seafloors. Geophys. Res. Lett. 35, L07611.

FAO, 2007. The world's mangroves, 1980–2005. Fao Forestry PaperFood and Agriculture Organization of the United Nations, Rome.

Hegge, B.J., Masselink, G., 1996. Spectral analysis of geomorphic time series: auto–spectrum. Earth Surf. Process. Landf. 21, 1021–1040.

Horstman, E.M., et al., 2011. Sediment dynamics in a mangrove creek catchment in Trang, Thailand. In: Shao, X., Wang, Z., Wang, G. (Eds.), Proceedings of the 7th IAHR Symposium on River, Coastal and Estuarine Morphodynamics, Beijing, pp. 675–685.

Horstman, E.M., Dohmen–Janssen, C.M., Hulscher, S.J.M.H., 2013. Flow routing in mangrove forests: a field study in Trang Province, Thailand. Cont. Shelf Res. 71, 52–67.

Kathiresan, K., Rajendran, N., 2005. Coastal mangrove forests mitigated tsunami. Estuar. Coast. Shelf Sci. 65, 601–606.

Kerr, A.M., Baird, A.H., Campbell, S.J., 2006. Comments on "coastal mangrove forests mitigated tsunami" by k. Kathiresan and n. Rajendran [estuar. Coast. Shelf sci. 65 (2005) 601–606]. Estuar. Coast. Shelf Sci. 67, 539–541.

Massel, S.R., Furukawa, K., Brinkman, R.M., 1999. Surface wave propagation in mangrove forests. Fluid Dyn. Res. 24, 219–249.

Mazda, Y., Magi, M., Kogo, M., Hong, P.N., 1997a. Mangroves as a coastal protection from waves in the Tong King delta, Vietnam. Mangrove Salt Marshes 1, 127–135.

Mazda, Y., et al., 1997b. Drag force due to vegetation in mangrove swamps. Mangrove Salt Marshes 1, 193–199.

Mazda, Y., Magi, M., Ikeda, Y., Kurokawa, T., Asano, T., 2006. Wave reduction in a mangrove forest dominated by *Sonneratia* sp. Wetlands Ecol. Manag. 14, 365–378.

McIvor, A.L., Möller, I., Spencer, T., Spalding, M., 2012. Reduction of Wind and Swell Waves by Mangroves. Cambridge Coastal Research Unit, Cambridge.

Mendez, F.J., Losada, I.J., 2004. An empirical model to estimate the propagation of random breaking and nonbreaking waves over vegetation fields. Coast. Eng. 51, 103–118.

Méndez, F.J., Losada, I.J., Losada, M.A., 1999. Hydrodynamics induced by wind waves in a vegetation field. Journal of Geophysical Research: Oceans 104, 18383–18396.

Möller, I., 2012. Bio-physical linkages in coastal wetlands — implications for coastal protection. In: Kranenburg, W.M., Horstman, E.M., Wijnberg, K.M. (Eds.), NCK-days 2012. Crossing borders in coastal research, Enschede, The Netherlands, pp. 51–60.

Möller, I., Spencer, T., French, J.R., Leggett, D.J., Dixon, M., 1999. Wave transformation over salt marshes: a field and numerical modelling study from north Norfolk, England. Estuar. Coast. Shelf Sci. 49, 411–426.

Paul, M., Amos, C.L., 2011. Spatial and seasonal variation in wave attenuation over *Zostera noltii*. J. Geophys. Res. Oceans 116, C08019.

Quartel, S., Kroon, A., Augustinus, P.G.E.F., Van Santen, P., Tri, N.H., 2007. Wave attenuation in coastal mangroves in the red river delta, Vietnam. J. Asian Earth Sci. 29, 576–584.

Spalding, M., Kainuma, M., Collins, L., 2010. World Atlas of Mangroves. Earthscan, London, UK.

Suzuki, T., Zijlema, M., Burger, B., Meijer, M.C., Narayan, S., 2012. Wave dissipation by vegetation with layer schematization in swan. Coast. Eng. 59, 64–71.

Thai Meteorological Department, 2012. The climate of Thailand, Climatological Group, Meteorological Development Bureau, Thai Meteorological Department, Bangkok, Thailand.

Ting, C.L., Lin, M.C., Cheng, C.Y., 2004. Porosity effects on non-breaking surface waves over permeable submerged breakwaters. Coast. Eng. 50, 213–224.

Van Loon, A.F., Dijksma, R., Van Mensvoort, M.E.F., 2007. Hydrological classification in mangrove areas: a case study in Can Gio, Vietnam. Aquat. Bot. 87, 80–82.

Van Rijn, L.C., 2008. Principles of Fluid Flow and Surface Waves in Rivers, Estuaries, Seas and Oceans. Aqua Publications, The Netherlands.

Van Santen, P., Augustinus, P.G.E.F., Janssen-Stelder, B.M., Quartel, S., Tri, N.H., 2007. Sedimentation in an estuarine mangrove system. J. Asian Earth Sci. 29, 566–575.

Vo-Luong, H.P., Massel, S.R., 2006. Experiments on wave motion and suspended sediment concentration at Nang Hai, Can Gio mangrove forest, southern Vietnam. Oceanologia 48, 23–40.

Vo-Luong, H.P., Massel, S.R., 2008. Energy dissipation in non-uniform mangrove forests of arbitrary depth. J. Mar. Syst. 74, 603–622.

Watson, J.G., 1928. Mangrove forests of the Malay peninsula. Malayan Forest Records No. 6 Federated Malay States Government, Kuala Lumpur.

Winterwerp, J.C., de Graaff, R.F., Groeneweg, J., Luijendijk, A.P., 2007. Modelling of wave damping at Guyana mud coast. Coast. Eng. 54, 249–261.

Winterwerp, J.C., Erftemeijer, P.L.A., Suryadiputra, N., Eijk, P., Zhang, L., 2013. Defining eco-morphodynamic requirements for rehabilitating eroding mangrove-mud coasts. Wetlands 33, 515–526.

Woodroffe, C.D., 1992. Mangrove sediments and geomorphology. In: Robertson, A.I., Alongi, D.M. (Eds.), Tropical Mangrove Ecosystems. American Geophysical Union, Washington DC, pp. 7–41.